Atmos. Chem. Phys. Discuss., 15, 34063–34090, 2015
www.atmos-chem-phys-discuss.net/15/34063/2015/
doi:10.5194/acpd-15-34063-2015

Atmospheric Chemistry and Physics Discussions
Open Access

Marine boundary layer structure as observed by space-based Lidar

T. Luo, Z. Wang, and D. Zhang

University of Wyoming, Dept. Atmospheric Science, Laramie, WY, USA

Received: 23 October 2015 – Accepted: 24 November 2015 – Published: 3 December 2015

Correspondence to: Z. Wang (zwang@uwyo.edu)

Published by Copernicus Publications on behalf of the European Geosciences Union.

Abstract

The marine boundary layer (MBL) structure is important to the exchange of heat, momentum, and moisture between oceans and the low atmosphere and to the marine low cloud processes. This paper explores MBL structure over the eastern Pacific region with a new 4 year satellite-based dataset. The MBL aerosol lidar backscattering from the CALIPSO (Cloud-Aerosol Lidar and Infrared Pathfinder Satellite Observations) was used to identify the MBL top (BLH) and the mixing layer height (MLH). Results showed that MBL is generally decoupled with MLH/BLH ratio ranging from ~ 0.5 to ~ 0.8 and the MBL decoupling magnitude is mainly controlled by estimated inversion strength (EIS) that affects the cloud top entrainment process. The systematic differences between drizzling and non-drizzling stratocumulus tops, which may relate to the meso-scale circulations or gravity wave in MBL, also show dependence on EIS. Further analysis indicated that the MBL shows similar decoupled structure for clear sky and cumulus cloud-topped conditions, but is better mixed under stratiform cloud breakup and overcast conditions.

1 Introduction

The planetary boundary layer is the lowest part of the troposphere that is directly influenced by the Earth's surface and is important for the exchange of heat, momentum, and moisture between the surface and the upper troposphere (Stull, 1988). Over oceans, the marine boundary layer (MBL) clouds are frequently present within the MBL, with significant contributions to the energy and moisture budgets of the earth due to their high albedo (Klein and Hartmann, 1993; Norris and Leovy, 1994; Norris, 1998; Wood and Bretherton, 2004). With decades of research efforts, the MBL cloud is still one of the primary contributors to the uncertainty in the model predictions of climate change (Bony and Dufresne, 2005; Randall et al., 2007; Wyant et al., 2015). Due to the close interactions of MBL clouds with the vertical structure and turbulence of the MBL, the

Discussion Paper | Discussion Paper | Discussion Paper | Discussion Paper |

ACPD

15, 34063–34090, 2015

Marine boundary layer structure as observed by space-based Lidar

T. Luo et al.

representation of convection and MBL processes are critical to the successful simulations of climate (Randall et al., 1985; Albrecht et al., 1995; Bony and Dufresne, 2005; Wyant et al., 2010; Zhang et al., 2011).

The MBL is often decoupled and thus is not well mixed (Bretherton and Wyant, 1997; Wood and Bretherton, 2004; Jone et al., 2011; Caldwell et al., 2012). The MBL is frequently decoupled at the downwind of the subtropical stratocumulus regions (Bretherton and Wyant, 1997; Wood and Bretherton, 2004; Jone et al., 2011). Deeper MBL (higher than 1 km) are more likely to be decoupled (Wood and Bretherton, 2004). The MBL decoupling is controlled by a wide rage of factors. Bretherton and Wyant (1997) suggested that the decoupling structure is mainly driven by an increasing ratio of the surface latent heat flux to the net radiative cooling in the cloud, and other factors, such as drizzle, the vertical distribution of radiative cooling in the cloud, and sensible heat fluxes, only play less important roles. However, Zhou et al. (2015) showed that the entrainment of the dry warm air above the inversion could be the dominant factor triggering the systematic decoupling, while surface latent heat flux, precipitation, and diurnal circulation did not play major roles.

The MBL structure and processes are still not well understood. Early observations are mainly limited to specific case studies (Wood and Bretherton, 2004). The boundary layer structure can be derived from ground-based observations such as sounding (Seidel et al., 2010) or lidar (Emeis et al., 2008). However, ground-based observations of the MBL over the global oceans are sparse and may be not representative. Wood and Bretherton (2004) firstly tried a combination of MODIS and reanalysis data to study the MBL decoupling, though the passive remote sensing cannot give the direct measurement of MBL structures.

New satellite-based observations open new ways to observe the boundary layer structure. The global boundary layer height (BLH) climatology were derived by using Global Positioning System radio occultation (GPS RO) measurements (Ratnam and Basha, 2010; Guo et al., 2011; Ao et al., 2012), the Lidar In-space Technology Experiment (LITE) (Randall et al., 1998), the Geoscience Laser Altimeter System (GLAS)

(Palm et al., 2005), and the Cloud-Aerosol Lidar with Orthogonal Polarization (CALIOP) (Jordan et al., 2010; McGrath-Spangler and Denning, 2012, 2013). GPS RO provides a valuable global view of height-resolved refractivity or moisture structure of boundary layer, but suffers with very coarse spatial resolutions (200 m in vertical and ~ 200 km horizontal) and insufficient penetration into the lowest 500 m of atmosphere (Xie et al., 2012). Satellite-based lidar is sensitive to boundary layer aerosols and clouds, and can provide global measurements of aerosol properties and their vertical distributions. The aerosol vertical distribution in the boundary layer is heavily influenced by the boundary layer thermal structure, therefore, aerosol structures were uses as a good proxy to study the MBL structures (Stull and Eloranta, 1984; Boers et al., 1984; Melfi et al., 1985; Boers and Eloranta, 1986; Leventidou et al., 2013; Luo et al., 2014a; Kong and Fan, 2015).

Former studies have shown that satellite-based lidar has the great ability to derive global BLH distributions (Randall et al., 1998; Palm et al., 2005; Jordan et al., 2010; McGrath-Spangler and Denning, 2012, 2013), especially by using CALIOP observations, which have much finer vertical (30 m) and horizontal resolution (333 m) in the lower tropospheric measurements. The gradient or variance methods over land and ocean under all-sky or no-optically-thick-cloud conditions were used in those studies. However, over ocean, the BLH is associated with the aerosol layer top (clear sky) or stratiform cloud top (cloudy sky), while a well mixed-layer usually exists bellow the BLH with a strong gradient in aerosol loading near the mixed layer height (MLH) under decoupled MBL conditions (Luo et al., 2014a). The former studies did not fully consider the MBL decoupled structure in choosing lidar methodology, therefore, having a potential to report MLH as BLH. In MBL, cumulus cloud top heights are often higher than BLH. Difficulties in identifying the stratiform clouds could lead to BLH uncertainties. Those issues could result in statistical biases in marine BLH distributions and thus different value and pattern of the BLH over ocean reported among those studies.

By fully considering MBL decoupling structure, a new CALIOP based approach was developed to reliably determine BLH and MLH to investigate the clear-sky MBL de-

ACPD
15, 34063–34090, 2015

couple structure (Luo et al., 2014a). This paper will use the new method to CALIOP observations to investigate the MBL decouple structure over the eastern Pacific Ocean region, and combine with reliable cloud type identification to provide BLH information under stratiform-cloud-topped conditions. Section 2 describes the data used in this study. Section 3 introduces and evaluates the lidar MBL structure identification methodology with the ship-base observations. Section 4 presents the results and discussions, and brief conclusions are in Sect. 5.

2 Data

2.1 Satellite observations and data collocation

Multiple remotely sensed and operational meteorological datasets over eastern Pacific Ocean regions during the period of June 2006 to December 2010 are used in this study.

The cloud-free CALIOP measured aerosol backscattering was used to identify the MBL structure. CALIOP, carried on the Cloud-Aerosol Lidar and Infrared Pathfinder Satellite Observations (CALIPSO), is a dual-wavelength (532 and 1064 nm) backscatter lidar operating a polarization channel at 532 nm (Winker et al., 2007, 2009). The along-track footprint of CALIOP is 333 m and the vertical resolution is 30 m below 8.2 km. CALIOP level 1B data provide three calibrated and geolocated lidar profiles of 532 and 1064 nm total attenuated backscatter (TAB) and 532 nm perpendicular polarization component. The molecular backscattering was estimated by the temperature and pressure profiles from the ECMWF-AUX (European Center for Medium range Weather Forecasting AUX-algorithm, Partain, 2004).

The 2B-CLDCLASS-LIDAR (Wang et al., 2013) provides the cloud top height (CTH) and cloud type with combining CloudSat and CALIOP observations to better identify the cloud boundaries. The cloudy CALIOP profiles were removed from further averaging, and the cloudy BLH was estimated from the CTH of marine stratiform clouds, which were a good proxy to estimate marine BLH under cloudy conditions as widely used in the previous studies (Minnis et al., 1992; Wood and Bretherton, 2004; Ahlgrimm and Randall, 2006; Zuidema et al., 2009; Karlsson et al., 2010). To classify the cloudy MBL into drizzle and non-drizzle categories, drizzle was detected with CloudSat Profiling Radar (CPR) measured reflectivity factor in CloudSat 1B-CPR product (Tanelli et al., 2008) with a threshold of −20 dB (Leon et al., 2008).

The atmosphere large-scale stability parameters used in this study include lower tropospheric stability (LTS, Klein and Hartmann, 1993), the difference of potential temperature between 700 hPa and the surface ($\theta_{700} - \theta_{1000}$), and estimated inversion strength (EIS) (Wood and Bretherton, 2006). EIS subtracts the moist adiabatic lapse rate multiplied by the depth between 700 hPa and the LCL (lifting condensation level) from the LTS, and therefore more closely reveals the strength of a possible inversion. These stability parameters were estimated from AIRS (the Atmospheric Infrared Sounder) level 2 version 5 products (Jason, 2008). AIRS, onboard on Aqua, is a grating spectrometer having a spectral resolution of $\nu/\Delta\nu \approx 1200$, a total of 2378 channels in the range of 3.7–15.4 µm with a few spectral gaps, and provides well-calibrated level 1B radiances (Overoye, 1999). AIRS is co-registered with AMSU (Pagano et al., 2003; Lambrigtsen and Lee, 2003), and the combined measurements are used to retrieve temperature, humidity and numerous other surface and atmospheric parameters. Geophysical retrievals are obtained in clear sky and broken cloud cover using a cloud-clearing methodology (Susskind et al., 2003).

The ocean surface meteorological parameters were obtained from AMSR-E Level 3 daily Ocean Products version-5. The daily AMSR-E Ocean Products are produced by Remote Sensing Systems (RSS, http://www.remss.com/). Sea surface temperature (SST) and surface wind speed at 10 m ($U_{10\,\mathrm{m}}$) from AMSR-E are used in this study. The orbital data is mapped to 0.25° grid box and is divided into 2 maps based on ascending and descending passes. The root mean square difference in SST retrievals is 0.76 K, and the RMS difference in wind speed retrievals is 0.92 m s^{-1} with a bias of 0.57 m s^{-1} (Wentz et al., 2003).

ACPD
15, 34063–34090, 2015

All the related datasets were collocated into AMSR-E 25 km footprint and cloud-free CALIOP backscattering profiles are then averaged. Only data over the eastern Pacific Ocean (within 40° N and 40° S, eastern than 50° W, and with 200 km away from continents) were used in the following analyses. The MBL aerosol identifications are same as Luo et al. (2014a).

2.2 MAGIC and collocated satellite observations

The Marine ARM GPCI Investigation of Clouds (MAGIC) field campaign (http://www.arm.gov/sites/amf/mag/) deployed the US Department of Energy (DOE) Atmospheric Radiation Measurement Program Mobile Facility 2 (AMF2) on the commercial cargo container ship Horizon Spirit from October 2012 through September 2013 with 20 round trips (Lewis et al., 2012; Zhou et al., 2015). The MAGIC transect is the line from the coast of California to Hawaii (35.8° N, 125.8° W to 18° S, 173.8° W) to provide unprecedented, intra-seasonal, high-resolution ship-based observations to improve our understanding of the Sc-to-Cu (Stratocumulus-to-Cumulus) transition along this transect. The AMF2 contains a state-of-the-art instrumentation suite and was designed to operate in a wide range of climate conditions and locations, including shipboard deployments.

This study mainly used the atmospheric soundings and MARMETX (marine meteorological measurements) datasets to characterize MBL structure. Standard radiosondes (Vaisala model MW-31, SNE50401) were launched every 6 h to measure vertical profiles of the thermodynamic state of the atmosphere (temperature, pressure, relative humidity, and wind speed and direction). The MARMETX dataset (http://www.arm.gov/campaigns/amf2012magic/) contains standard surface meteorological parameters measured by the MARMET: temperature (T), pressure (P), relative humidity (RH), and apparent and true wind speed and direction; and the sea surface skin temperature measured by the Infrared Sea surface Temperature Autonomous Radiometer (ISAR) with an accuracy of better than 0.18 °C.

ACPD
15, 34063–34090, 2015

Title Page
Abstract | Introduction
Conclusions | References
Tables | Figures
◄ | ►
◄ | ►
Back | Close
Full Screen / Esc
Printer-friendly Version
Interactive Discussion

To evaluate the satellite-retrieved MBL structure with results from MAGIC soundings, the cloud-free CALIOP observations from October 2012 through September 2013 were collocated to MAGIC soundings within 2.5° grid-box. The cloud information was provided by the gradient method (Wang and Sassen, 2001) and then cloud-free CALIOP profiles within 25 km grids were averaged to improve the signal-to-noise ratio.

The high spectral resolution lidar (HRSL, Shipley et al., 1983; Piironen and Eloranta, 1994) measured total attenuated backscattering was also used to document the aerosol and cloud distributions. Due to the high occurrence of the cloud along the MAGIC transect, the lidar-based MBL structure identification method was not applied to the HRSL observations.

3 MBL structure identification methodology

3.1 MBL structure identification methodology for SONDE

For SONDE, the BLH was determined by the Richardson number (RI) method (with the Eq. 2 in Vogelezang and Holtslag, 1996), which determines the BLH as the height at which RI is larger than the critical value (= 0.25). The RI method is suitable for both stable and convective boundary layers. This method relates the derived BLH to boundary layer processes – surface heating, wind shear and capping inversion, thus gives the BLH more physical meaning. Also RI method is not strongly dependent on sounding vertical resolution, giving no-negative BLH. Therefore BLH derived by the RI method will be used as the best estimation to evaluate lidar based BLH estimations (Hennemuth and Lammert, 2006; Seidel et al., 2010).

The MLH detection method was determined based on the MBL structure observed in MAGIC. Figure 1 presents the one transect of MAGIC measurements of HSRL and potential temperatire. It clearly shows that the BLHs with RI method usually correspond with the aerosol layer top, or stratiform clouds top over the stratiform cloud region (eastern than longitude of $\sim -137°$) and sometimes with the highest cumulus clouds top over the cumulus cloud region (western than longitude of ∼ $-137°$). Over cumulus cloud region, the MBL becomes obviously decoupled, and there is usually one or more inversion layers below the RI determined BLH. The first inversion layer (from bottom up) usually limits the upward transportation of the aerosols to form a layer below with more concentrated aerosols than that above, and can limit the vertical developments of the small cumulus clouds formed in the mixing layer. This characteristic indicates that to the MLH height can be identified as the base of the first inversion layer with inversion strength larger than 0.05 K/100 m in SONDE potential temperature profiles.

3.2 MBL structure identification methodology for CALIOP

As detailed in Luo et al. (2014b), the BLH can be determined with an improved threshold method with threshold $\beta'_{\mathrm{thr}} = \beta'_m + 2 \cdot \mathrm{MBV}$ in collocated CALIOP level 1B data. Here, is the molecular backscattering, estimated by temperature and pressure profiles from ECMWF-AUX products; MBV is the measured backscatter variation, estimated as the standard deviation of measured attenuated backscatter coefficients from 30 to 40 km. The MLH was identified by the gradient method (Luo et al., 2014b). The gradient of aerosol backscattering is calculated after three points moving smoothing. Then, the MLH is determined from bottom up as the first point with aerosol backscattering gradient larger than 2 times of the molecular backscattering gradient.

Figure 2 shows the comparisons of MBL structure between SONDE and CALIOP measurements. The mean MBL structure by CALIOP and SONDE along the MAGIC transect is shown in Fig. 2a. Both results show similar trend of the MBL structure, that is, less decoupled near the coast and more decoupled over the far ocean. The CALIOP-derived BLH and MLH are biased lower than those from SONDE. Over the stratiform cloud regions, the CALIOP-derived MBL structure is more decoupled than SONDE results. Those differences are mainly resulted from the limited sampling and spatial mismatch. As shown in Fig. 1, the soundings were measured over all-sky conditions, while only cloud-free CALIOP profiles can be used to derive the MBL structure. Especially over the stratiform cloud region where the cloud fraction in the MBL is very high (Fig. 1), the collocated cloud-free CALIOP profiles are often too far from the sounding observations. However, the CALIOP-derived BLH and MLH show good agreement with those from SONDE as shown in Fig. 2b. The bias and root mean square error (RMSE) in CALIOP-derived BLH is -0.14 ± 0.37 km, and -0.1 ± 0.45 km in MLH. Furthermore, as shown in Fig. 2b, the SONDE-derived MLH agrees well with the LCL, with the bias and RMSE of -0.13 ± 0.21 km. We further compared the CALIOP-derived BLH and stratiform CTHs (CTH_{sc}) within the same AMSR-E grid box over the eastern Pacific Ocean region, as shown in Fig. 2d. The result shows good agreements with each other with the bias and RMSE of -0.06 ± 0.52 km. These evaluations indicate the good accuracies of our CALIOP based BLH and MLH determinations for MBL structure study.

4 Results and discussions

4.1 MBL structure over the eastern Pacific Ocean

In this section, we will investigate the MBL structure over the eastern Pacific Ocean with the 4 year new MBL and marine boundary layer cloud (MBLC) dataset as built in the last section. Figure 3 shows the 4 year mean MBL structure (BLH, MLH and MLH/BLH), CTH_{sc} with or without drizzle, EIS and $U_{10\,m}$ over the eastern Pacific Ocean. Here and after, the MBL structure (BLH, MLH and MLH/BLH) is referred to the clear-sky condition with aerosols as a proxy, while the CTHsc is used as the proxy of BLH under cloudy conditions.

The 4 year mean BLH over the eastern Pacific Ocean is shown in Fig. 3a. Figure 3a shows that the marine BLH is low than ~ 1 km near the coast region at latitude of $\sim \pm 30°$ due to the strong subsidence. When going far away from the strong subsidence region, the BLH increases. The BLH is high over the Intertropical Convergence Zone (ITCZ) due to the strong convection and large-scale convergence, especially over eastern Pacific near the Central America. However, along the equator, the BLH is low and shows increase tendency when westward. The 4 year mean MLH (Fig. 3b) shows a similar pattern to the BLH. The general increasing trend of BLH when away from the coast was also illustrated in former satellite-based studies (Ratnam and Basha, 2010; Guo et al., 2011; Ao et al., 2012; Randall et al., 1998; Palm et al., 2005; Jordan et al., 2010; McGrath-Spangler and Denning, 2012, 2013). However, there are significant magnitude differences between our study and former studies due to different methodologies associated with different definition of BLH and the filtering of cloud conditions. For example, the BLH reported in McGrath-Spangler and Denning (2013) show a quite similar pattern and value over the eastern Pacific Ocean with the MLH in our result.

The 4 year mean MBL coupling status in terms of MLH/BLH is shown in Fig. 3c. The larger the MLH/BLH is, the better mixed the MBL is. The MBL is better mixed (with higher MLH/BLH) in the stratiform cloud dominated region (where Sc Fraction $>\sim 0.4$ with stronger EIS and lower BLH) than in the cumulus cloud dominated region (where Sc Fraction $<\sim 0.4$ with weaker EIS and higher BLH). The MBL is obviously decoupled over the ITCZ but shows better mixing in the equator. However, the MBL becomes more decoupled westward along the equator.

The stratiform cloud occurs more frequently (Sc fraction $>\sim 0.6$) when EIS $>\sim 1$ K, with decreasing fraction towards the far ocean, as shown in Fig. 3d. Figure 3e and f show the drizzled and non-drizzled stratiform cloud top. The stratiform cloud case is defined as the case with only stratiform cloud (and clear-sky if it has) profiles in the collocated 25 km grid-box. The drizzled stratiform cloud case is the stratiform cloud case with at least one drizzled stratiform cloud profile in the collocated 25 km grid-box. The non-drizzled stratiform case is the stratiform cloud case with non-precipitating at all. The drizzled stratiform cloud tops are lower than ~ 1.5 km near the coast where the stratus cloud is dominated, and are increasing up to ~ 2.5 km when far away from the coast. The non-drizzled stratiform cloud top shows the similar pattern as the drizzled stratiform cloud top, except that the non-drizzled stratiform cloud top is decreasing

ACPD
15, 34063–34090, 2015

when approaching the central tropic Pacific. The drizzled Sc top is ~ 0.2 to 1 km higher than the non-drizzle Sc top, which suggests the important role of the mesoscale circulations in MBL. The precipitation favors updraft regions and the breakup of Sc usually happens in downdrafts area and thus with less precipitations, which could also be observed in the rift area of Sc (Sharon et al., 2006) and in MAGIC (Zhou et al., 2015). Furthermore, among clear-sky MBL cases (cases in Fig. 3a) with stratiform clouds in the same 25 km grid-box, the occurrence of drizzled stratiform cloud case is ~ 6.2 % (the number of drizzled stratiform cloud profiles/the number of stratiform cloud profiles), while the occurrence of drizzled stratiform cloud case is ~ 32 % for all MBL cases. The stratiform cloud case containing clear-sky profile relates to the broken Sc clouds or near the cloud edge. Therefore, it indicates that the drizzle less happens in broken Sc clouds or near the cloud edge.

The detailed assessments of the seasonal MBL and MBLC structures in the two selected transects over the northeastern and southeastern Pacific Ocean (NPO and SPO) are presented in Figs. 4 and 5. Figures 4 and 5a1–a4 show the seasonal mean MBL structure in terms of MBL aerosol loading, overlaid with seasonal mean BLH and MLH. Seen from the mean BLH, MLH and their standard variations, the MBL tends to be more frequently well mixed near the coast region and be more frequently decoupled over the far ocean, corresponding to the stronger EIS near the coast and weaker EIS over the far ocean (the black diamond-solid lines in Figs. 4 and 5b1–b4). The seasonal variations in the MBL structure are both small over the NPO and SPO regions, except that the MBL tends to be lower and better mixed near the coast region in MAM and JJA over the NPO, and in JJA and SON over the SPO, associated with the stronger EIS (> 5 K) than EIS (< 5 K) in the other seasons.

For sea salt aerosols, the surface wind speed is the main factor controlling the loading near the surface, while its vertical distribution closely relates to the boundary layer processes (Luo et al., 2014b). Seen from Figs. 4 and 5, when far away from the coast, the aerosol loading (contours in Figs. 4 and 5a1–a4) in the lower well-mixed layer shows good positive correlation with the $U_{10\,\mathrm{m}}$ in NPO but not the case in SPO. In SPO, when eastern than longitude of $\sim -100^{\circ}$, the aerosol loading in the lower well-mixed layer is increasing with decreasing of the $U_{10\,\mathrm{m}}$ because the MLH is decreasing and limits the vertical transportation. When near the coast, the aerosol loading in the well-mixed layer has weak correlation with the $U_{10\,\mathrm{m}}$ over both regions, possibly due to the aerosol transported from the continent.

Figures 4 and 5c1–c4 show the mean Sc and drizzle occurrences over the two regions, as the black diamond solid line and blue circle-solid line respectively. Over the NPO region (Fig. 4c1–c4), the Sc occurrence is small near the coast and increases to the maximum of ~ 0.6 near the latitude of $\sim 28^{\circ}$ N, and then decreases when southward to the tropic. The Sc occurrence over the NPO shows less correlation with EIS, which has a generally decreasing trend when far away from the coast. Over the SPO region (Fig. 5c1–c4), the Sc occurrence and the EIS correlate well with each other with both decreasing when far away from the coast. The drizzle occurrence showed less correlation with EIS in both regions.

Figures 4 and 5d1–d4 show the seasonal mean $\mathrm{CTH_{drizzle}}$ (blue diamond line) and $\mathrm{CTH_{no\ drizzle}}$ (green diamond line) over the two regions, along with the seasonal mean BLH and MLH. The $\mathrm{CTH_{drizzle}}$ is higher than BLH, while the $\mathrm{CTH_{no\ drizzle}}$ is close to the BLH. In JJA and SON, the $\mathrm{CTH_{drizzle}}$ shows a negative correlation with the EIS. However, in DJF and MAM, the $\mathrm{CTH_{drizzle}}$ shows a weaker correlation with the EIS, especially over NPO region. The $\mathrm{CTH_{no\ drizzle}}$ generally shows a weak correlation with the EIS, although there is a positive correlation with the EIS, such as over the SPO when western than longitude of $\sim -90^{\circ}$ in DJF and MAM and when western than longitude of $\sim 100^{\circ}$ in JJA and SON. The difference between $\mathrm{CTH_{drizzle}}$ and $\mathrm{CTH_{no\ drizzle}}$ shows strong dependence on the EIS, i.e., smaller difference associated with stronger EIS, and larger difference associated with weaker EIS.

The MBL and MBLC activities are strongly connected with the large-scale stabilities. Figure 6 shows the relationships between EIS and MBL coupling structure. As seen in Fig. 6a, both observations from MAGIC SONDE and CALIOP show that the MBL tends to be better mixed with increasing EIS. According to the definition of EIS, it has the same physical meaning to the inversion strength near the mixed layer top, which is one of the main parameters controlling the entrainment process (Venzenten et al., 1999). The stronger EIS is, the stronger the inversion near the MBL top is, and the weaker the entrainment of the dry warm air above the inversion is. Therefore, the relationship between EIS and MBL structure indicates that the entrainment of the dry warm air above the inversion can be the main factor controlling the MBL decoupling. It could also be expected that the wind shear and surface heat flux could also be important for the MBL decoupling, which can also affect the entrainment process (Venzenten et al., 1999). However, further analyses with $U_{10\,\mathrm{m}}$ and SST showed only very weak correlations with MBL coupling structure, possibly due to the uncertainties in satellite retrievals of these parameters. Instead, we found that the MBL coupling structure is controlled by both LTS and EIS when EIS $<\sim 3\,\mathrm{K}$, that is, better mixed with increasing of EIS and decreasing of LTS, as shown in Fig. 6b.

The differences of drizzling and non-drizzling Sc tops are also controlled by the EIS, as indicated by the seasonal mean relationship between EIS and $\mathrm{CTH}_{\text{no drizzle}}/\mathrm{CTH}_{\text{drizzle}}$ in Fig. 6c. The seasonal mean relationship between EIS and MLH/BLH is also plotted in Fig. 6c. When EIS $< 0\,\mathrm{K}$, mean $\mathrm{CTH}_{\text{no drizzle}}/\mathrm{CTH}_{\text{drizzle}}$ does not vary with EIS. When EIS $> 0\,\mathrm{K}$, the relative difference between $\mathrm{CTH}_{\text{drizzle}}$ and $\mathrm{CTH}_{\text{no drizzle}}$ becomes larger with decreasing EIS, indicating more vigorous the subsidence and uplifting in the lower troposphere under weak EIS conditions. And with increasing EIS, the relative difference between $\mathrm{CTH}_{\text{drizzle}}$ and $\mathrm{CTH}_{\text{no drizzle}}$ becomes smaller, associated with stronger subsidence, and more coupled and shallower MBL. The role of inversion strength in modulating Sc top suggests that the subsidence and uplifting may relate to meso-scale processes, such as gravity waves, which can be generated from the geostrophic adjustment, jet break or other sources, and affect the morphology of clouds (Jiang and Wang, 2012; Allen et al., 2013).

ACPD
15, 34063–34090, 2015

4.2 Discussion

The MBL decoupling was suggested to play an important role in Sc–Cu transition (Bretherton and Wyant, 1997; Wood and Bretherton, 2004). The mean MBL structures in term of aerosol backscattering under clear, stratiform cloud and Cu cloud conditions are shown in Fig. 7. The clear condition is defined as totally cloud-free in the 25 km AMSR-E footprint (named as clear MBL). Those cases are expected to be less affected by the local circulation associated with the cloud development. The stratiform cloud condition is defined as partially cloudy and with only stratiform cloud and clear sky in the 25 km AMSR-E footprint (named as stratiform MBL). The Cu cloud condition is defined as partially cloudy and with only Cu cloud and clear sky in the 25 km AMSR-E footprint (named as Cu MBL). It is assumed that the cloud-topped MBL can have the similar structure to the nearby clear-sky MBL within the 25 km footprint for the Sc and Cu MBL cases. The vertical gradients of TAB show that the clear and Cu MBL become more decoupled with increasing BLH and decreasing EIS. The Sc MBL shared similar characteristics but are better mixed than clear and Cu MBL when EIS > 0. According to Fig. 3, the region with EIS < 0 K is the Cu cloud dominated region where the fraction of Sc cloud is smaller than 0.2, and the Sc MBL cases here are more likely to associated with the clear-sky MBL adjacent to the small stratiform. The region of $0 <$ EIS < 2.5 K is transition region where the Sc clouds are broken and transit to Cu clouds. The Sc MBL cases with $0 <$ EIS < 2.5 K are more possibly associated to the clear-sky MBL adjacent to broken Sc. The Sc MBL cases with EIS > 2.5 K are more possibly associated with the clear-sky MBL near the edge of overcast Sc in the region where Sc fraction $>\sim 0.6$. When EIS < 0 K, the stratiform MBL showed no major difference with clear and Cu MBL. With increasing EIS, corresponding to increasing amount of stratiform clouds, the increasing of large-scale subsidence prompts the well-mixed MBL, and sometimes decoupled MBL with two well-mixed sub-layers (Fig. 7c2).

ACPD
15, 34063–34090, 2015

5 Conclusions

This paper used 4 year satellite observations to investigate the MBL decouple structure over the eastern Pacific region. The aerosol information in CALIOP-measured backscattering can be a good proxy to determine the MBL decoupled structure. The aerosol layer top is a good indicator for BLH and could be identified by the threshold method. The MLH could be identified by the gradient methods. The lidar determined BLH showed good agreements with RI method determined BLH from sounding measurements and stratiform cloud top. The lidar determined MLH showed good agreement with the MLH determined by the first inversion layer base in sounding profile.

The lidar methodology was applied to the 4 year satellite observations over the eastern Pacific Ocean. The cloud-free MBL structure characteristics were analyzed together with the stratiform cloud top as the cloudy MBL top. For the first time, the climatology and seasonal variations of the MBL structure in the region were presented and analyzed. Results showed that MBL is generally decoupled with MLH/BLH ratio ranging from ~ 0.5 to ~ 0.8 and the MBL decoupling magnitude is mainly controlled by EIS that affects the cloud top entrainment process. The systematic differences between drizzling and non-drizzling Sc tops, which may relate to the mesoscale circulations driven by gravity wave in MBL, also show dependence on EIS. Further analysis showed that the MBL shows similar decoupled structure for clear sky and Cumulus cloud-topped conditions, but is better mixed for Sc breakup and overcast conditions.

This study demonstrated that satellite lidar measurements offer a unique opportunity to characterize MBL over large scale, which is no possible through other measurements. With other possible measurements, multi-satellite measurements also offer a chance to further study related MBL processes. Observational results presented here will be valuable to evaluate and improve model MBL simulations under different dynamical and thermodynamical conditions.

ACPD
15, 34063–34090, 2015

Acknowledgements. This research was partially funded by the DOE Grant DE-SC0006974 as part of the ASR program and by the NASA Grant NNX13AQ41G. The authors acknowledge the US Department of Energy ARM Climate Research Facility.

References

Ahlgrimm, M. and Randall, D. A.: Diagnosing monthly mean boundary layer properties from reanalysis data using a bulk boundary layer model, J. Atmos. Sci., 63, 998–1012, 2006.

Albrecht, B. A., Jensen, M. P., and Syrett, W. J.: Marine boundary layer structure and fractional cloudiness, J. Geophys. Res., 100, 14209–14222, 1995.

Allen, G., Vaughan, G., Toniazzo, T., Coe, H., Connolly, P., Yuter, S. E., Burleyson, C. D., Minnis, P., and Ayers, J. K.: Gravity-wave-induced perturbations in marine stratocumulus, Q. J. Roy. Meteor. Soc., 139, 32–45, 2013.

Ao, C. O., Waliser, D. E., Chan, S. K., Li, J.-L., Tian, B., Xie, F., and Mannucci, A. J.: Planetary boundary layer heights from GPS radio occultation refractivity and humidity profiles, J. Geophys. Res., 117, D16117, doi:10.1029/2012JD017598, 2012.

Boers, R. and Eloranta, E. W.: Lidar measurements of the atmospheric entrainment zone and potential temperature jump across the top of the mixed layer, Bound.-Lay. Meteorol., 34, 357–375, 1986.

Boers, R., Eloranta, E. W., and Coulter, R. L.: Lidar observations of mixed layer dynamics: tests of parameterized entrainment models of mixed layer growth rate, J. Clim. Appl. Meteorol., 23, 247–266, 1984.

Bony, S. and Dufresne, J.-L.: Marine boundary layer clouds at the heart of tropical cloud feedback uncertainties in climate models, Geophys. Res. Lett., 32, L20806, doi:10.1029/2005GL023851, 2005.

Bretherton, C. S. and Wyant, M. C.: Moisture transport, lower-tropospheric stability, and decoupling of cloud-topped boundary layers, J. Atmos. Sci., 54, 148–167, 1997.

Emeis, S., Schafer, K., and Munkel, C.: Surface-based remote sensing of the mixing-layer height – a review, Meteorol. Z., 17, 621–630, 2008.

Guo, P., Kuo, Y.-H., Sokolovskiy, S. V., and Lenschow, D. H.: Estimating atmospheric boundary layer depth using COSMIC radio occultation data, J. Atmos. Sci., 68, 1703–1713, 2011.

Jason, L.: README Document for AIRS Level-2 Version 005 Standard Products, Goddard Earth Sciences Data And Information Services Center, National Aeronautics and Space Administration (NASA), Greenbelt, MD, USA, 2008.

Jiang, Q. and Wang, S.: Impact of gravity waves on marine stratocumulus variability, J. Atmos. Sci., 69, 3633–3651, 2012.

Jones, C. R., Bretherton, C. S., and Leon, D.: Coupled vs. decoupled boundary layers in VOCALS-REx, Atmos. Chem. Phys., 11, 7143–7153, doi:10.5194/acp-11-7143-2011, 2011.

Jordan, N. S., Hoff, R. M., and Bacmeister, J. T.: Validation of Goddard Earth Observing System-version 5 MERRA planetary boundary layer heights using CALIPSO, J. Geophys. Res., 115, D24218, doi:10.1029/2009JD013777, 2010.

Klein, S. A. and Hartmann, D. L.: The seasonal cycle of low stratiform clouds, J. Climate, 6, 1587–1606, 1993

Kong, W. and Fan, Y.: Convective boundary layer evolution from lidar backscatter and its relationship with surface aerosol concentration at a location of a central China megacity, J. Geophys. Res.-Atmos., 120, 7928–7940, 2015.

Lambrigtsen, B. H. and Lee, S.-Y.: Coalignment and synchronization of the AIRS instrument suite, IEEE T. Geosci. Remote, 41, 343–351, 2003.

Leon, D. C., Wang, Z., and Liu, D.: Climatology of drizzle in marine boundary layer clouds based on 1 year of data from CloudSat and Cloud-Aerosol Lidar and Infrared Pathfinder Satellite Observations (CALIPSO), J. Geophys. Res., 113, D00A14, doi:10.1029/2008JD009835, 2008.

Leventidou, E., Zanis, P., Balis, D., Giannakaki, E., Pytharoulis, I., and Amiridis, V.: Factors affecting the comparisons of planetary boundary layer height retrievals from CALIPSO, ECMWF and radiosondes over Thessaloniki, Greece, Atmos. Environ., 74, 360–366, 2013.

Lewis, E. R., Wiscombe, W. J., Albrecht, B. A., Bland G. L., Flagg, C. N., Klein, S. A., Kollias, P., Mace, G., Reynolds, R. M., Schwartz, S. E., Siebesma, A. P., Teixeira, J., Wood, R., and Zhang, M.: MAGIC: Marine ARM GPCI Investigation of Clouds, DOE / SC-ARM-12-020, US Department of Energy, Washington, DC, USA, 12 pp., 2012.

Luo, T., Yuan, R., and Wang, Z.: Lidar-based remote sensing of atmospheric boundary layer height over land and ocean, Atmos. Meas. Tech., 7, 173–182, doi:10.5194/amt-7-173-2014, 2014a.

Luo, T., Yuan, R. M., and Wang, Z.: On factors controlling marine boundary layer aerosol optical depth, J. Geophys. Res.-Atmos., 119, 3321–3334, 2014b.

McGrath-Spangler, E. L. and Denning, A. S.: Estimates of North American summertime planetary boundary layer depths derived from space-borne lidar, J. Geophys. Res., 117, D15101, doi:10.1029/2012JD017615, 2012.
McGrath-Spangler, E. L. and Denning, A. S.: Global seasonal variations of midday planetary boundary layer depth from CALIPSO space-borne LIDAR, J. Geophys. Res.-Atmos., 118, 1226–1233, 2013.
Melfi, S. H., Sphinhirne, J. D., Chou, S. H., and Palm, S. P.: Lidar observations of the vertically organized convection in the planetary boundary layer over the ocean, J. Clim. Appl. Meteorol., 24, 806–821, 1985.
Minnis, P., Heck, P. W., Young, D. F., Fairall, C. W., and Snider, J. B.: Stratocumulus cloud properties derived from simultaneous satellite and island-based instrumentation during FIRE, J. Appl. Meteorol., 31, 317–339, 1992.
Norris, J. R.: Low cloud type over the ocean from surface observations. Part I: Relationship to surface meteorology and the vertical distribution of temperature and moisture, J. Climate, 11, 369–382, 1998.
Norris, J. R. and Leovy, C. B.: Interannual variability in stratiform cloudiness and sea surface temperature, J. Climate, 7, 1915–1925, 1994.
Overoye, K., Aumann, H. H., Weiler, M. H., Gigioli, G. W., Shaw, W., Frost, E., and McKay, T.: Test and calibration of the AIRS instrument, Proc. SPIE, 3759, 254–265, 1999.
Pagano, T. S., Aumann, H. H., Hagan, D. E., and Overoye, K.: Prelaunch and in-flight radiometric calibration of the Atmospheric Infrared Sounder (AIRS), IEEE T. Geosci. Remote, 41, 265–273, 2003.
Palm, S. P., Benedetti, A., and Spinhirne, J.: Validation of ECMWF global forecast model parameters using GLAS atmospheric channel measurements, Geophys. Res. Lett., 32, L22S09, doi:10.1029/2005GL023535, 2005.
Partain, P.: Cloudsat ECMWF-AUX Auxiliary Data Process Description and Interface Control Document, Cooperative Institute for Research in the Atmosphere, Colorado State University, Fort Collins, CO, USA, 2004.
Piironen, P. and Eloranta, E. W.: Demonstration of a high spectral resolution lidar based on an iodine absorption filter, Opt. Lett., 19, 234–236, 1994.
Randall, D. A., Abeles, J. A., and Corsetti, T. G.: Seasonal simulations of the planetary boundary layer and boundary-layer stratocumulus clouds with a general circulation model, J. Atmos. Sci., 42, 641–675, 1985.

Randall, D. A., Shao, Q., and Branson, M.: Representation of clear and cloudy boundary layers in climate models, in: Clear and Cloudy Boundary Layers, edited by: Holtslag, A. A. M. and Duynkerke, P. G., Royal Netherlands Academy of Arts and Sciences, Amsterdam, the Netherlands, 305–322, 1998.

Randall, D. A., Wood, R. A., Bony, S., Colman, R., Fichefet, T., Fyfe, J., Kattsov, V., Pitman, A., Shukla, J., Srinivasan, J., Stouffer, R. J., Sumi, A., and Taylor, K. E.: Climate models and their evaluation, in: Climate Change 2007: the Physical Science Basis, contribution of Working Group I to the Fourth Assessment Report of the Intergovernmental Panel on Climate Change, edited by: Solomon, S., Qin, D., Manning, M., Chen, Z., Marquis, M., Averyt, K. B., Tignor, M., and Miller, H. L., Cambridge University Press, Cambridge, UK and New York, NY, USA, 589–662, 2007.

Ratnam, M. V. and Basha, S. G.: A robust method to determine global distribution of atmospheric boundary layer top from COSMIC GPS RO measurements, Atmos. Sci. Lett., 11, 216–222, 2010.

Seidel, D. J., Ao, C. O., and Li, K.: Estimating climatological planetary boundary layer heights from radiosonde observations: comparison of methods and uncertainty analysis, J. Geophys. Res., 115, D16113, doi:10.1029/2009JD013680, 2010.

Shipley, S. T., Tracy, D. H., Eloranta, E. W., Trauger, J. T., Sroga, J. T., Roesler, F. L., and Weinman, J. A.: A high spectral resolution lidar to measure optical scattering properties of atmospheric aersols, Part I: Instrumentation and theory, Appl. Optics, 23, 3716–3724, 1983.

Stull, R. B. and Eloranta, E. W.: Boundary Layer Experiment 1983, B. Am. Meteorol. Soc., 65, 450–456, 1984.

Susskind, J., Barnet, C., Blaisdell, J., Iredell, L., Keita, F., Kouvaris, L., Molnar, G., and Chahine, M.: Accuracy of geophysical parameters derived from Atmospheric Infrared Sounder/Advanced Microwave Sounding Unit as a function of fractional cloud cover, J. Geophys. Res., 111, D09S17, doi:10.1029/2005JD006272, 2006.

Tanelli, S., Durden, S. L., Im, E., Pak, K. S., Reinke, D. G., Partain, P., Haynes, J. M., and Marchand, R. T.: CloudSat's cloud profiling radar after two years in orbit: Performance, calibration, and processing, IEEE T. Geosci. Remote, 46, 3560–3573, 2008.

Vanzanten, M. C., Duynkerke, P. G., and Cuijpers, J. W.: Entrainment parameterization in convective boundary layers, J. Atmos. Sci., 56, 813–828, 1999.

Vogelzang, D. and Holtslag, A.: Evaluation and model impacts of alternative boundary-layer height formulations, Bound.-Layer Meteorol., 81, 245–269, 1996.

ACPD
15, 34063–34090, 2015

Wentz, F. J., Gentemann, C., and Ashcroft, P.: On-orbit calibration of AMSR-E and the retrieval of ocean products, in: 83rd AMS Annual Meeting, American Meteorological Society, 9–14 February 2003, Long Beach, CA, USA, P 5.9, 2003.
Winker, D. M., Hunt, W. H., and McGill, M. J.: Initial performance assessment of CALIOP, Geophys. Res. Lett., 34, L19803, doi:10.1029/2007GL030135, 2007.
Winker, D. M., Vaughan, M. A., Omar, A., Hu, Y., Powell, K. A., Liu, Z., Hunt, W. H., and Young, S. A.: Overview of the CALIPSO mission and CALIOP data processing algorithms, J. Atmos. Ocean. Tech., 26, 2310–2323, 2009.
Wood, R. and Bretherton, C. S.: Boundary layer depth, entrainment, and decoupling in the cloud-capped subtropical and tropical marine boundary layer, J. Climate, 17, 3576–3588, 2004.
Wood, R. and Bretherton, C. S.: On the relationship between stratiform low cloud cover and lower-tropospheric stability, J. Climate, 19, 6425–6432, 2006.
Wyant, M. C., Wood, R., Bretherton, C. S., Mechoso, C. R., Bacmeister, J., Balmaseda, M. A., Barrett, B., Codron, F., Earnshaw, P., Fast, J., Hannay, C., Kaiser, J. W., Kitagawa, H., Klein, S. A., Köhler, M., Manganello, J., Pan, H.-L., Sun, F., Wang, S., and Wang, Y.: The PreVOCA experiment: modeling the lower troposphere in the Southeast Pacific, Atmos. Chem. Phys., 10, 4757–4774, doi:10.5194/acp-10-4757-2010, 2010.
Wyant, M. C., Bretherton, C. S., Wood, R., Carmichael, G. R., Clarke, A., Fast, J., George, R., Gustafson Jr., W. I., Hannay, C., Lauer, A., Lin, Y., Morcrette, J.-J., Mulcahy, J., Saide, P. E., Spak, S. N., and Yang, Q.: Global and regional modeling of clouds and aerosols in the marine boundary layer during VOCALS: the VOCA intercomparison, Atmos. Chem. Phys., 15, 153–172, doi:10.5194/acp-15-153-2015, 2015.
Xie, F., Wu, D. L., Ao, C. O., Mannucci, A. J., and Kursinski, E. R.: Advances and limitations of atmospheric boundary layer observations with GPS occultation over southeast Pacific Ocean, Atmos. Chem. Phys., 12, 903–918, doi:10.5194/acp-12-903-2012, 2012.
Zhang, C., Wang, Y., and Hamilton, K.: Improved representation of boundary layer clouds over the southeast Pacific in ARW-WRF using a modified tiedtke cumulus parameterization scheme, Mon. Weather Rev., 139, 3489–3513, 2011.
Zhou, X., Kollias, P., and Lewis, E. R.: Clouds, precipitation and marine boundary layer structure during the MAGIC field campaign, J. Climate, 28, 2420–2442, 2015.
Zuidema, P., Painemal, D., Szoeke, S., and de Fairall, C.: Stratocumulus cloud-top height estimates and their climatic implications, J. Climate, 22, 4652–4666, 2009.

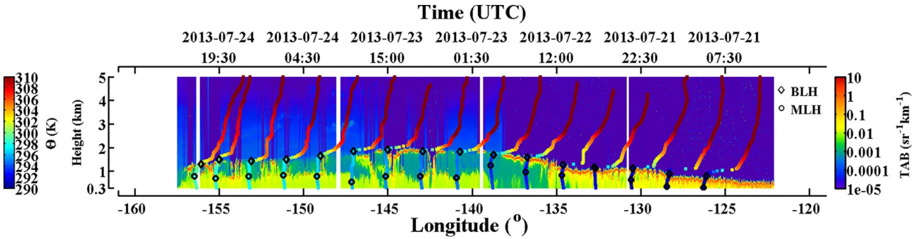

Figure 1. Potential temperature profiles and retrieved MBL structure (magenta diamonds for BLH and magenta circles for MLH) for a MAGIC leg from 21–24 July 2013, overlaid with total attenuated backscattering from HSRL.

ACPD
15, 34063–34090, 2015

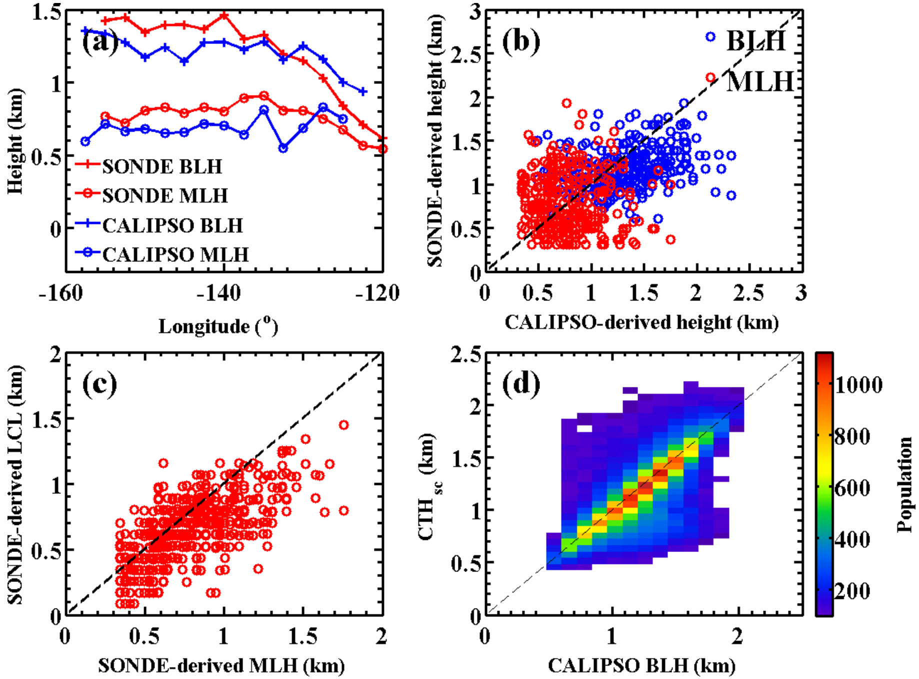

Figure 2. (a) Mean MBL structure along longitude from MAGIC sonde and collocated CALIOP observations; **(b)** comparisons of SONDE and CALIOP derived BLH and MLH; **(c)** comparison of SONDE derived MLH and LCL; **(d)** comparison of CALIOP derived BLH and stratiform cloud top (CTH_{sc}).

ACPD
15, 34063–34090, 2015

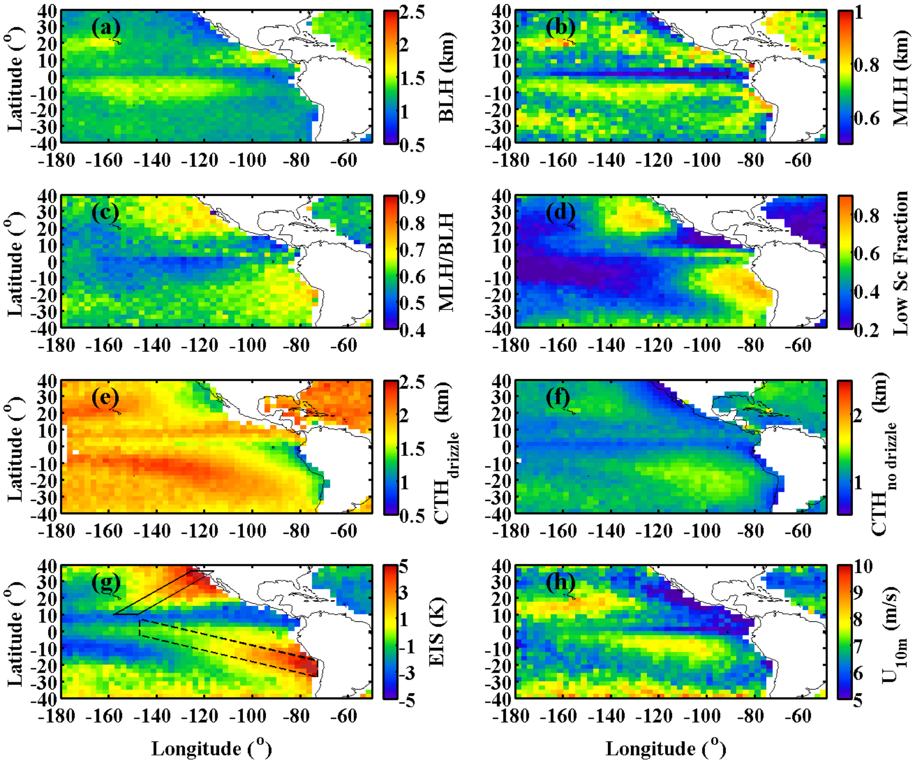

Figure 3. **(a)** CALIOP derived BLH; **(b)** CALIOP derived MLH; **(c)** CALIOP derived MBL decoupling structure in term of MLH/BLH; **(d)** Marine low clouds fraction; **(e)** drizzled stratiform CTH ($CTH_{drizzle}$); **(f)** non-drizzled stratiform CTH ($CTH_{no\ drizzle}$); **(g)** EIS; **(h)** $U_{10\,m}$. The solid and dashed boxes in panel **(g)** denote the selected transects on the northeastern and southeastern Pacific Ocean (NPO and SPO) used in Figs. 4 and 5 respectively.

ACPD
15, 34063–34090, 2015

Marine boundary layer structure as observed by space-based Lidar

T. Luo et al.

Title Page
Abstract Introduction
Conclusions References
Tables Figures
◀◀ ▶▶
◀ ▶
Back Close
Full Screen / Esc
Printer-friendly Version
Interactive Discussion

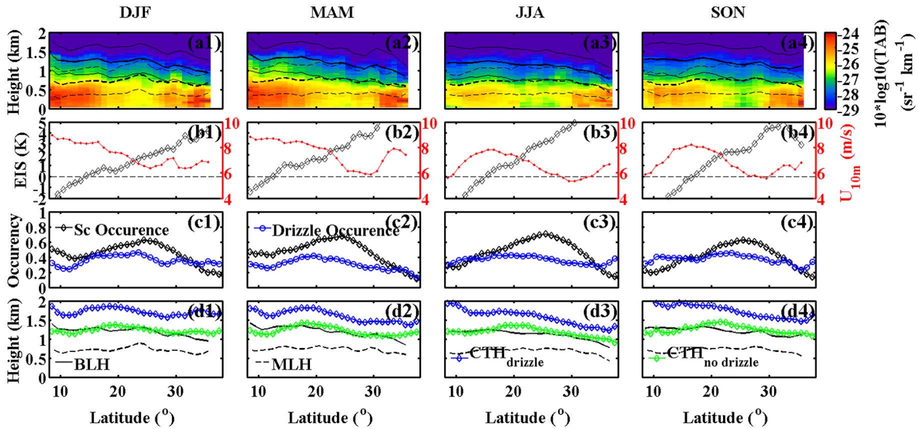

Figure 4. The satellite MBL observations along the transect region on the northeastern Pacific Ocean (NPO, solid box in Fig. 3e) in different seasons: **(a1)–(a4)** the mean BLH (solid line) and MLH (dashed line) overlaid with TAB, and corresponding standard derivations (thin solid and dashed lines); **(b1)–(b4)** EIS (black diamond line) and $U_{10\,\mathrm{m}}$ (red dot line); **(c1)–(c4)** stratocumulus (Sc) and drizzle occurrence; **(d1)–(d4)** comparisons of BLH, MLH, $\mathrm{CTH}_{\mathrm{drizzle}}$, and $\mathrm{CTH}_{\mathrm{no\ drizzle}}$. Drizzle occurrence is defined as the drizzling cloud profile number divided by the total cloud profile number.

ACPD
15, 34063–34090, 2015

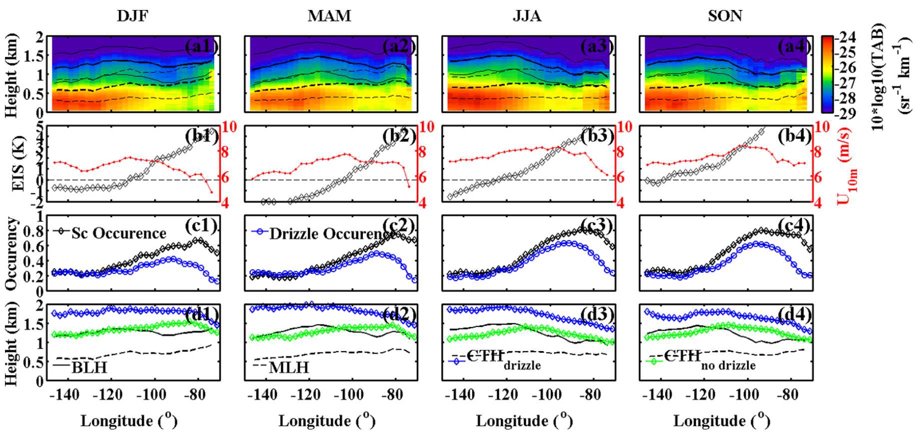

Figure 5. Same as Fig. 4 but for the transect region on the southeastern Pacific Ocean (SPO, dashed box in Fig. 3e) in different seasons.

ACPD
15, 34063–34090, 2015

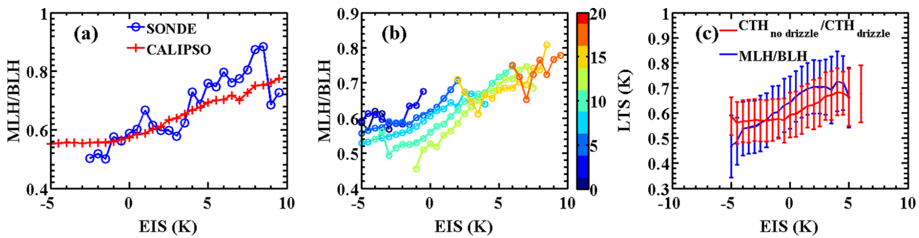

Figure 6. (a) Relationship with EIS and MLH/BLH in MAGIC and collocated Satellite observations; **(b)** relationship between EIS and MLH/BLH under different LTS over the eastern Pacific Ocean; **(c)** seasonal mean relationship between EIS with MLH/BLH and $CTH_{no\ drizzle}/CTH_{drizzle}$ over the eastern Pacific Ocean.

ACPD
15, 34063–34090, 2015

Marine boundary layer structure as observed by space-based Lidar

T. Luo et al.

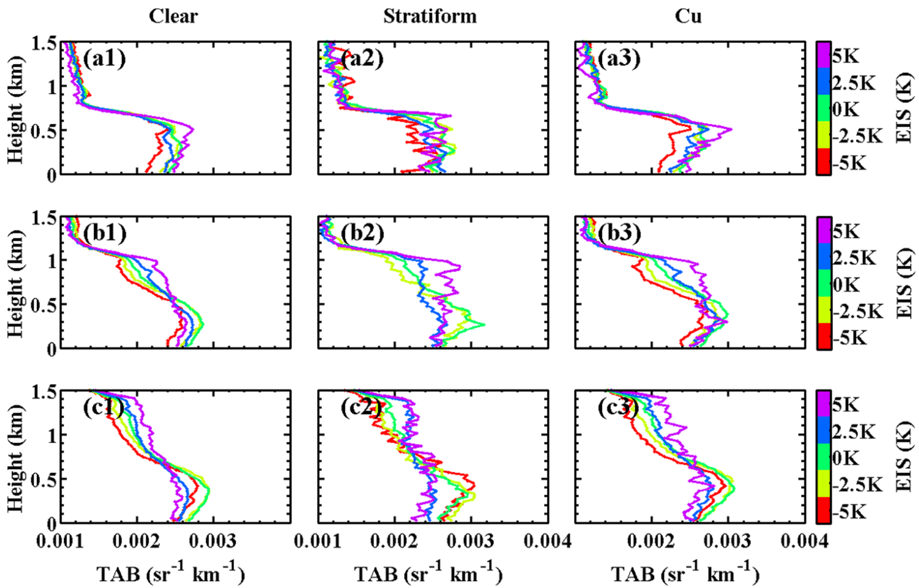

Figure 7. Mean MBL CALIOP TAB structure under different conditions: 0.6 < BLH < 0.8 km **(a1, a2, a3)**, 1 < BLH < 1.2 km **(b1, b2, b3)**, and 1.4 < BLH < 1.6 km **(c1, c2, c3)**. Panels **(a1, b1, c1)** are under the clear conditions that is defined as totally cloud-free over 25 km AMSR-E footprint; panels **(a2, b2, c2)** are under the stratiform cloud conditions that is defined as with only stratiform cloud and clear sky in each 25 km AMSR-E footprint; panels **(a3, b3, c3)** are under the Cu cloud conditions that is defined as with only Cu cloud and clear sky in each 25 km AMSR-E footprint. Only results with $5 < U_{10\,\mathrm{m}} < 8\,\mathrm{m\,s^{-1}}$ were included.

ACPD
15, 34063–34090, 2015

Marine boundary layer structure as observed by space-based Lidar

T. Luo et al.